De-Lin Huang
State Key Lab of Mechanical System
and Vibration,
Shanghai Jiaotong University,
Shanghai 200240, China;
School of Mechanical Engineering,
Shanghai Jiaotong University,
Shanghai 200240, China
e-mail: cjwanan@sjtu.edu.cn

Shi-Chang Du[1]
State Key Lab of Mechanical System
and Vibration,
Shanghai Jiaotong University,
Shanghai 200240, China;
School of Mechanical Engineering,
Shanghai Jiaotong University,
Shanghai 200240, China
e-mail: lovbin@sjtu.edu.cn

Gui-Long Li
School of Mechanical Engineering,
Shanghai Jiaotong University,
Shanghai 200240, China
e-mail: lgllg68629315@qq.com

Zhuo-Qi Wu
School of Mechanical Engineering,
Shanghai Jiaotong University,
Shanghai 200240, China
e-mail: zqwu@sjtu.edu.cn

A Systematic Approach for Online Minimizing Volume Difference of Multiple Chambers in Machining Processes Based on High-Definition Metrology

The volume variation of multiple chambers of a workpiece is one of the most important factors that can directly influence the performance of the final product. This paper presents a novel systematic approach for online minimizing the volume difference of multiple chambers of a workpiece based on high-definition metrology (HDM). First, the datum of high-density points is transformed by a random sample consensus (RANSAC) algorithm due to its good robustness in fitting. Second, a procedure containing reconstruction of interior curved surfaces of chambers, boundary extraction, and projection is developed to calculate the accurate volumes of the multiple chambers. Third, a model for obtaining an optimized machining parameter for depth of chambers is explored to minimize the volume difference of any two ones of all the chambers. The model is formulated as a multi-objective optimization (MOO) problem, and a new procedure of multi-objective particle swarm optimization (MOPSO) algorithm is developed to solve this problem. Finally, a milling depth is output as the optimal milling parameter for controlling the volume variation of multiple chambers. The results of a case study show that the proposed approach can minimize the volume difference of four combustion chambers of a cylinder head and it can be well applied online in volume variation control of multiple chambers in machining processes. [DOI: 10.1115/1.4035897]

Keywords: volume variation control, high-definition metrology, multiple chambers, optimization model, multi-objective particle swarm optimization

1 Introduction

The chamber volumes are very important for some mechanical products. For instance, the volume variations of engine cylinder head combustion chambers (see Fig. 1) directly affect the compression ratio of an engine. The interior surfaces of the chambers are usually not being machined after casting processes due to high machining cost, such as large gasoline engine and small gasoline engines from Shanghai Automotive Industry Corporation and General Motors company in Shanghai, China, EA888 engine from Shanghai Volkswagen automobile company in Shanghai, China, and N12 and B12 engines from Shanghai Automotive Industry Corporation General Motors Wuling company in Liuzhou, China are not being machined with the technology of machining interior surfaces of a combustion chamber. Traditional titration methods are frequently applied offline to evaluate the variations of chamber volumes in machining processes since they are considerably time-consuming (tens of minutes), and also, the measurement accuracy is limited to the proficiency level of an operator. It is difficult to online measure and control the volume variation of multiple chambers of a workpiece in machining processes.

With the development of online HDM technologies, great opportunities are provided for online controlling flat surface variation and volume variation of a workpiece. A representative of online HDM for flat surface variation is Shapix [1], which is based on laser holographic interferometry metrology. Several researches about online controlling flat surface variation based on HDM have been conducted. Du et al. [2–4] proposed a shearlet-based method and support vector machine-based methods to

separate and extract different surface components using HDM. Du and Fei [5] also presented a co-Kriging method based on multivariate spatial statistics to estimate surface form error using HDM. Wang et al. [6–8] developed a modified gray level co-occurrence matrix to extract features from the images converted from face-milled surface measured by HDM. Suriano et al. [9] proposed a new methodology for efficiently measuring and monitoring flat surface variations by fusing in-plant multiresolution measurements and process information. Nguyen et al. [10] presented a method to reduce flat surface variation in face-milling processes based on HDM measurements. However, ShaPix can only be applied for measuring the flat surfaces, but it cannot be directly used to measure the volume of a chamber. Recently, a new HDM technology using laser triangulation metrology is developed for online measuring the volume variation of multiple chambers. For example, for each interior surface of four chambers of a cylinder head, more than 2×10^6 measured points (called high-density point clouds) (see Fig. 2) can be obtained, and the whole measurement time is within 80 s.

Although several methods applicable to the flat surface variation control have been explored based on HDM, they cannot be directly used to control the volume variation of multiple chambers. The control of volume variations based on HDM is confronted with three main difficulties:

(1) *Datum transformation*: For the online measurement machine, *XY* plane of the sensor coordinate system is regarded as the datum plane of the obtained point cloud, but the map of partial point cloud is not parallel to the underside of the workpiece. In order to extract the boundary of a chamber from the point cloud, *Z* coordinates of the point cloud of underside of the workpiece should be approximately zero. Therefore, it is necessary to transform
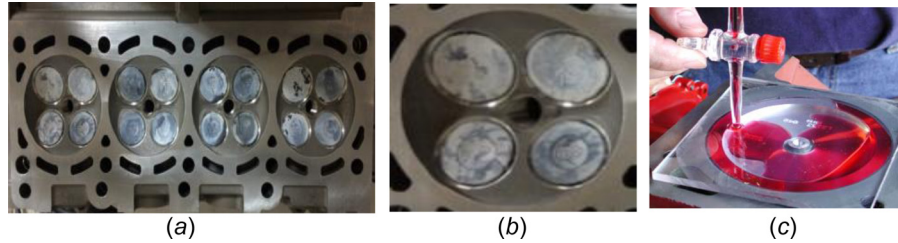
Fig. 1 A cylinder head with four combustion chambers and offline volume measurement: (a) cylinder head, (b) a combustion chamber, and (c) titration methods

the datum plane of the point cloud. The conventional methods of plane fitting, such as the least-square (LS) method [11,12] and the characteristic value method [13], involve error analysis, but they cannot eliminate the abnormal points. Therefore, it is difficult to obtain an accurate datum plane of the point cloud.

(2) *Accurate volume calculation of multiple chambers*: Basically, there are several holes in the interior surfaces of the chambers. For instance, there is a spark hole plugged in the interior surface of an engine head combustion chamber. The hole can cause the missing of the point cloud in the interior surfaces, which adds difficulty to volume calculation of a chamber. Besides, since the interior surfaces of the chambers are irregular after casting processes, it is difficult to accurately calculate the volume of the chambers based on the three-dimensional coordinates of the point cloud.

(3) Search an optimized machining parameter for depth of chambers to minimize the volume difference of any two ones of all the chambers. Although the interior surfaces of the chambers of a workpiece are not being machined due to high machining cost, the underside of the workpiece usually needs to be milled and the milling parameter is closely related to the volumes of all the chambers. Therefore, it is desirable to obtain an optimized milling parameter to minimize the volume difference of any two ones of all the chambers. Taking a cylinder head as an example, there are n combustion chambers in a cylinder head and V_i is the volume of the ith chamber (see Fig. 3). It is unpractical to mill the interior surfaces of each chamber to make the volume of each combustion chamber equal the designed volume due to high machining cost. The combustion chamber volumes can only be controlled by milling the underside of the cylinder head. Therefore, the key to control the volume variation of multiple chambers is to determine the optimal milling parameter (depth h_0). The volume of each combustion chamber is measured by online HDM measurement machine, which consists of the merits of quick speed, high accuracy, and sequential point cloud. After the measurement, the milling parameter h_0 needs to be optimized to minimize the volume difference of any two ones of all the combustion chambers.

However, to the best of our knowledge, there has been no systematic approach for online minimizing volume difference of multiple chambers in machining processes based on HDM. This paper is intended to contribute to this end.

The remainder of this paper is organized as follows: In Sec. 2, a systematic approach is proposed to online minimize volume difference of multiple chambers in machining processes based on HDM. In Sec. 3, a case study is presented to validate the proposed approach. The result analysis is implemented to illustrate the performance of the proposed approach for volume variation control of multiple chambers. Finally, conclusions are given in Sec. 4.

2 The Proposed Approach

The framework of the proposed approach is shown in Fig. 4, and the main steps of this approach are described as follows:

Step 1: Collect three-dimensional and sequential point cloud of multiple chambers of a workpiece using online measurement machine.

Step 2: Develop an approach consisting of datum transformation, accurate volume calculation of multiple chambers, and a model obtaining an optimized machining parameter to minimize the volume difference of any two ones of all the chambers. First, the datum plane of the high-density points is transformed based on a RANSAC algorithm due to its good robustness in fitting; second, a procedure containing reconstruction of interior curved surface of chambers, boundary extraction, and projection is presented to calculate the accurate volumes of the multiple chambers based on the point cloud. Third, a model is developed to optimize the milling parameter of the underside of a multichamber workpiece to minimize the volume difference of any two ones of all the chambers. Finally, MOPSO algorithm is presented to solve the model.

Step 3: Output an optimized milling parameter (depth h_0) from the proposed approach, and the multichamber workpiece should be milled according to the output parameter.

2.1 Datum Transformation. In order to transform datum plane of the point cloud from XY plane of sensor coordinate system to the underside of a workpiece, the datum plane parameters of the point cloud based on sensor coordinate
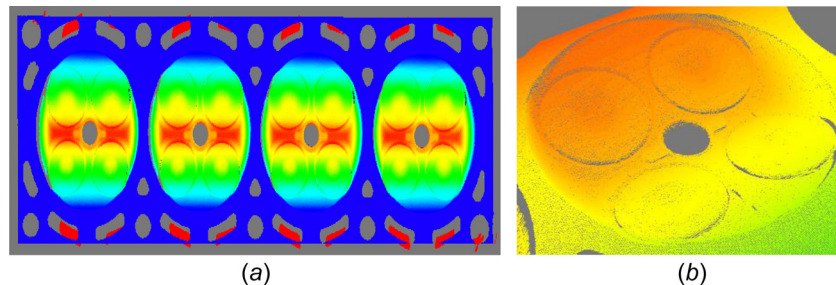

Fig. 2 High-density points measured by new HDM technology: (a) point cloud of a cylinder head and (b) point cloud of a combustion chamber
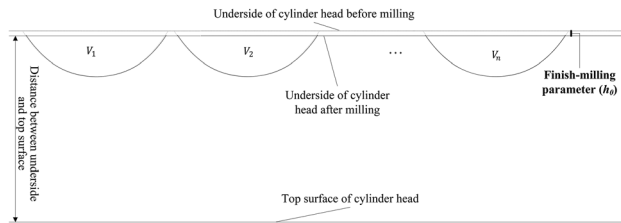
Fig. 3 Milling underside of cylinder head with *n* combustion chambers

system should be calculated. The collected point cloud includes not only all the points on the interior surface but also abnormal points as a result of the influence of measurement environment and reflection of surface finish. Therefore, there appears a problem about how to extract accurate datum plane from the point cloud with many abnormal points. To overcome this problem, a procedure based on RANSAC algorithm to calculate the parameters of the datum plane is explored. The structure of input data collected from a cylinder head by HDM sensor is shown in Fig. 5.

RANSAC algorithm can obtain a robust plane fitting result under the condition of a large number of abnormal points [14–16]. The description of RANSAC algorithm is shown in Fig. 6, and the main steps are described as follows:

Step 1: Randomly select three points from the point cloud and calculate the corresponding plane equation of the three points. The plane equation is expressed as $ax + by + cz + d = 0$. Here, a, b, c, and d are the parameters of the plane equation. Then, calculate the distance from arbitrary point P_i of the point cloud to the plane, and the distance ds_i is calculated by

$$ds_i = \frac{|ax_i + by_i + cz_i + d|}{\sqrt{a^2 + b^2 + c^2}} \quad (1)$$

Step 2: Determine the value of threshold t. The strategy to choose the threshold t is mentioned in Ref. [17]. If $d_i \leq t$, point P_i is considered as inner point of the obtained plane. Then, count the number (N) of the inner points of the plane.

Step 3: Repeat the above steps for n times and select a plane with the largest number of inner points.

Step 4: The selected plane is refitted with the largest number of inner points according to eigenvalue algorithm, and the final fitted plane equation is calculated.

Assume that the obtained plane equation is $Ax + By + Cz + D = 0$. The normal vector of the plane is (A, B, C), and the plane is through point $(0, 0, D/C)$. Then, the datum plane of the sensor coordinate system is represented as

$$\begin{cases} \mathbf{w}_1 = (1, 0, -C/A) \\ \mathbf{w}_3 = (A, B, C) \\ \mathbf{w}_2 = \mathbf{w}_3 \times \mathbf{w}_1 \end{cases} \quad (2)$$
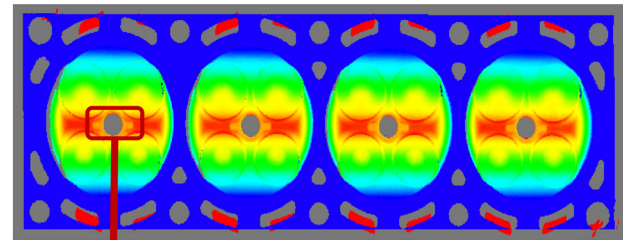
(a)
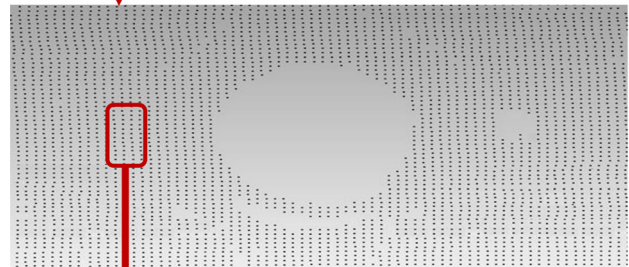
(b)

No.	X (mm)	Y (mm)	Z (mm)
18659	−9.203	146.492	8.136
18660	−9.564	146.495	8.040
18661	−9.925	146.498	7.945
18662	−10.285	146.501	7.850
18663	−10.645	146.503	7.759

(c)

Fig. 5 The structure of input data collected from a cylinder head: (*a*) point cloud collected from a cylinder head, (*b*) local distribution of the collected point cloud, and (*c*) the detailed form of the collected point cloud as input data

The Gram–Schmidt orthonormalization [18] is used to deal with the representation of sensor coordinate system (shown in Fig. 7). $a_1, a_2,$ and a_3 are regarded as the workpiece surface coordinate system, and $b_1, b_2,$ and b_3 are regarded as the sensor coordinate system. The datum transformation matrix H transforming datum plane from sensor coordinate system to the workpiece surface coordinate system is obtained by

$$\begin{cases} b_1 = a_1 \\ b_2 = a_2 - \dfrac{[b_1, a_2]}{[b_1, b_1]} b_1 \\ b_3 = a_3 - \dfrac{[b_1, a_3]}{[b_1, b_1]} b_1 - \dfrac{[b_2, a_3]}{[b_2, b_2]} b_2 \\ e_1 = \dfrac{1}{\|b_1\|} b_1, \; e_2 = \dfrac{1}{\|b_2\|} b_2, \; e_3 = \dfrac{1}{\|b_3\|} b_3 \\ H = [e_1, e_2, e_3] \end{cases} \quad (3)$$
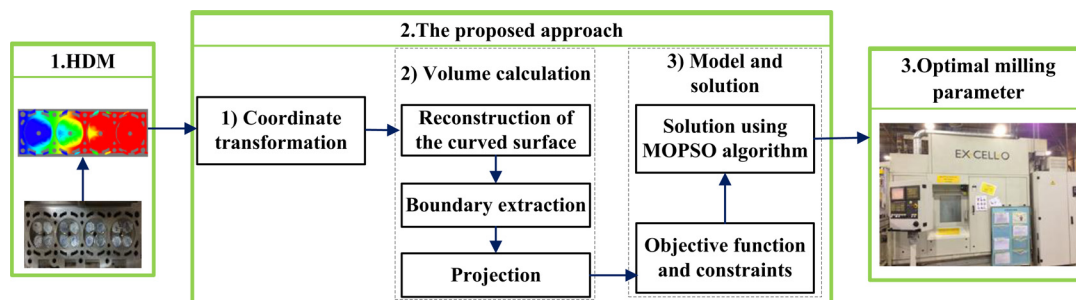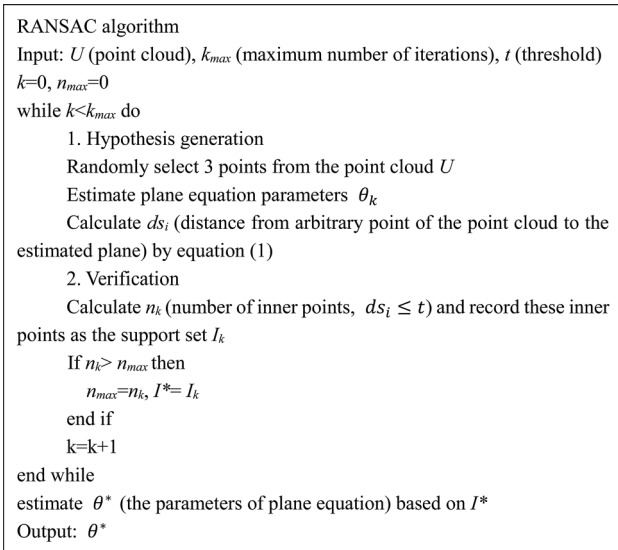

Fig. 4 The framework of the proposed approach

```
RANSAC algorithm
Input: U (point cloud), k_max (maximum number of iterations), t (threshold)
k=0, n_max=0
while k<k_max do
        1. Hypothesis generation
        Randomly select 3 points from the point cloud U
        Estimate plane equation parameters θ_k
        Calculate ds_i (distance from arbitrary point of the point cloud to the
estimated plane) by equation (1)
        2. Verification
        Calculate n_k (number of inner points, ds_i ≤ t) and record these inner
points as the support set I_k
        If n_k> n_max then
            n_max=n_k, I*= I_k
        end if
        k=k+1
end while
estimate θ* (the parameters of plane equation) based on I*
Output: θ*
```

Fig. 6   The description of RANSAC algorithm

For each point (P_i) of the point cloud, the transformation is conducted by

$$P'_i = \text{inv}(H) * P_i \qquad (4)$$

After the point cloud is transformed, the value of Z coordinate of each point is the distance from the point to the datum plane, and the value of Z coordinate of each point on the datum plane (workpiece surface) is approximately zero.

2.2   Accurate Volume Calculation of Multiple Chambers

2.2.1   Reconstruction of Interior Curved Surface. Due to the interference of the measuring environment and the influence of surface cleanliness of the cylinder head, there exist missing points in the collected point cloud (shown in Fig. 8). Besides, there are several holes of spark plug in the cylinder heads and they cannot be measured by the HDM system. The reflections of these holes are some relatively large blank areas in the point cloud (shown in Figs. 8 and 9).

The missing points and points that are not collected in the blank area are marked as null, and the interpolation is conducted based on the coordinates of the neighborhood points. Ranks of the weighted interpolation are developed to interpolate the points marked as null. The procedure of the interpolation is described as follows:

Step 1: Search each row of the point cloud for the first point P_i that is marked as null and record the location of the previous point P_{i-1}. The location of a point is the ordinal number of that point in a row. P_{i-1} is an adjacent point of P_i and it is not a null point.
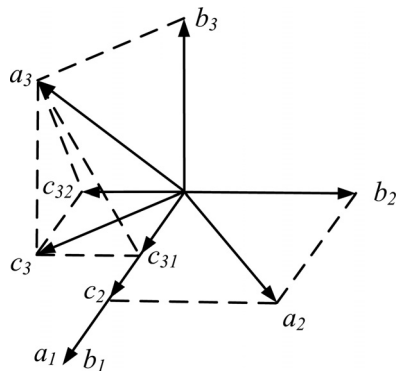

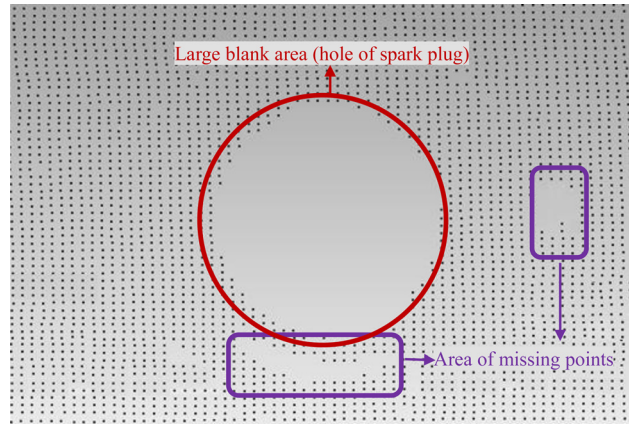**Fig. 7   An illustration of Gram–Schmidt transformation**

Fig. 8   Area of missing points in the collected point cloud

Step 2: Take point P_i as the starting point and search the same row for the first point P_j that is not marked as null and record the location of point P_j.

Step 3: For the $(j-i)$ points marked as null from point P_i to point P_j, the interpolation is conducted by

$$P_k = \frac{k}{j-i}(P_j - P_i) + P_i \quad (i-1 < k < j) \qquad (5)$$

where P_k is the point marked as null between points P_i and P_j.

Step 4: Repeat the above steps and complete interpolation of a row. There may need one more interpolation in a row since the missing points may form one more cluster in that row (shown in Fig. 10).

Step 5: Repeat steps 1–4 and complete interpolation of all the rows.

After the completion of the point cloud interpolation, the point cloud needs to be grid to generate interior curved surface of a chamber. The interpolated point cloud is complete and in order, which means that the number of points in each row and each column is the same. There is a corresponding topological relationship in the point cloud, that is, the locations of points in each row are fixed, and each point and its neighborhood can be quickly determined. Then, the point cloud mesh is built based on the locations of points in each row and each column of the point cloud.

The reconstruction process of the curved surface of the point cloud is shown in Fig. 11. For arbitrary point $P_{i,j}$ (point in ith row and jth column) of the sequential point cloud, connect its adjacent
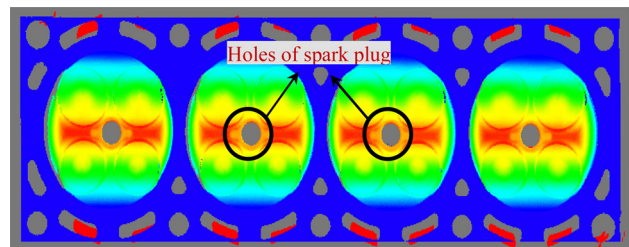

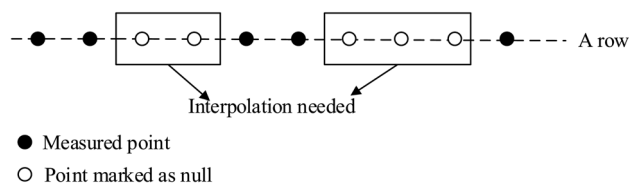**Fig. 9   Large blank areas in the collected point cloud**
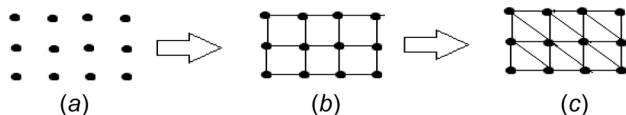

Fig. 10   Interpolations needed in a row

Fig. 11 Schematic diagram of structured point cloud mesh generation: (*a*) sequential point cloud, (*b*) quadrilateral mesh, and (*c*) triangular mesh
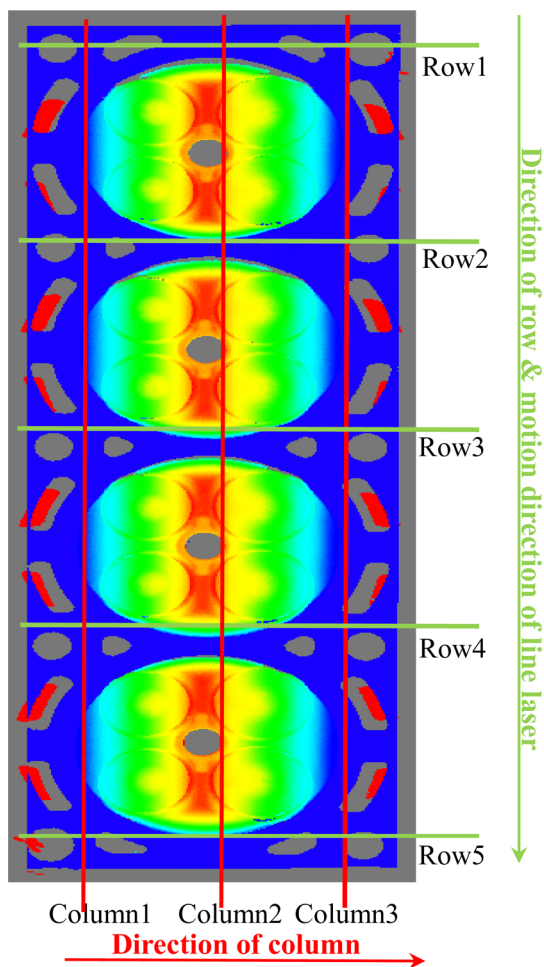

Fig. 12 Direction indications of row and column

points $P_{i+1,j}$ and $P_{i,j+1}$, and quadrilateral mesh is generated. On the basis of the quadrilateral mesh, connect the points $P_{i,j}$ and $P_{i+1,j+1}$, and the triangular mesh is also generated. At this point, the reconstruction of the curved surface is completed.

2.2.2 Boundary Extraction. After the completion of reconstruction of the curved surface, the effective area of a chamber on the underside of multichamber workpiece should be determined since it is the area where the reconstructed triangular meshes

project. The effective area of a chamber is the boundary of the chamber. Therefore, the boundary of a chamber should be extracted from the point cloud. The point cloud measured from the multiple chambers is sequential, and the point numbers of each row in the point cloud are the same. The direction indications of "row" and "column" in this study are shown in Fig. 12.

The initial row and terminal row of each chamber should be first determined from the point cloud in the scanning direction of the sensor of the online measurement machine. The Z coordinate value of a point approximates zero if the point is on the bottom surface where the boundaries of the multiple chambers lie. If not, the point is on the interior surface of the multiple chambers. Similarly, the average Z coordinate value of points in each row of the point cloud approximates zero if all the points in each row are on the surface where the boundaries of the multiple chambers lie. If not, there exists one or more points of a row, which are on the interior surface of the multiple chambers. Then, the average Z coordinate value of each row of the point cloud is calculated and the effect of abnormal points on the accuracy of boundary extraction can be eliminated by a statistical method. The average Z coordinate value of the kth row of the point cloud is calculated by the following equation:

$$Z_{k\mathrm{mean}} = \left(\sum Z_{km} \right) \Big/ n_k \qquad (6)$$

where Z_{km} is Z coordinate value of the mth point of the kth row of the point cloud, n_k is the point number of the kth row of the point cloud, and $Z_{k\mathrm{mean}}$ is the average Z coordinate value of the kth row of the point cloud.

The proposed process of boundary extraction of the multiple chambers is described as follows:

Step 1: Calculate the average Z coordinate value of the points in each row and make a statistical table that consists of the average Z coordinate value and sequence number of each row.

Step 2: Search the statistical table from middle to both sides. When the average Z coordinate value is approximately zero for the first time, the corresponding rows are the initial row and terminal row (shown in Fig. 13).

Step 3: Search boundary points of each row from the determined initial row to terminal row. Since the Z coordinate values of points in each of the searched rows obey the same rule of average Z coordinate value of each row in step 2, search the boundary points from middle to both sides of each row between the determined initial row to terminal row.

Step 4: Since each column also follows the same rules that are shown in steps 1–3, the boundary points of each column can be found.

Step 5: Combine the boundary points of each row and each column, and these boundary points form the boundary of each chamber.

2.2.3 Projection. Based on the triangular meshes of the chamber interior surface and the determination of chamber boundary, the volume of a chamber is calculated by projection. The underside of a multichamber workpiece is selected as a projection plane, and the triangular meshes are projected to it, constituting many convex pentahedrons within the extracted boundary. The volume of the chamber is the sum of volumes of all the convex pentahedrons.
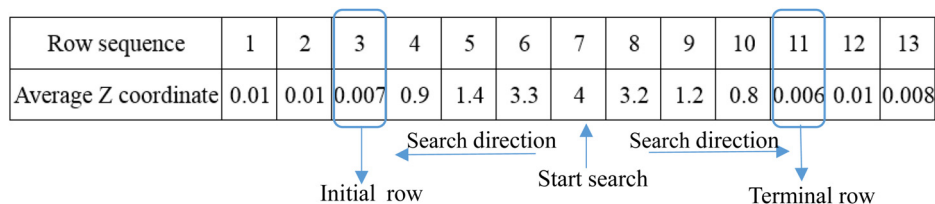
Row sequence	1	2	3	4	5	6	7	8	9	10	11	12	13
Average Z coordinate	0.01	0.01	0.007	0.9	1.4	3.3	4	3.2	1.2	0.8	0.006	0.01	0.008

Fig. 13 An illustration of determining initial row and terminal row
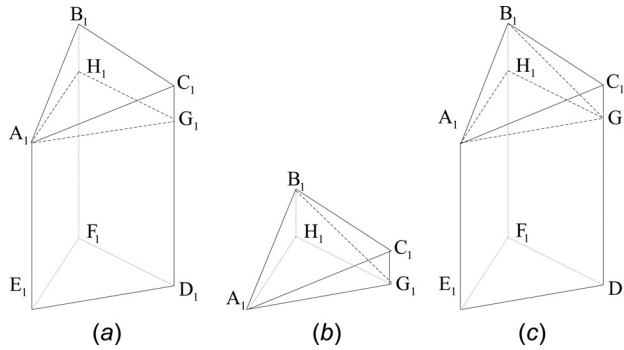
Fig. 14 Segmentation of convex pentahedron

where $h_{A_1E_1}$ is the distance between the plane of $E_1F_1D_1$ and the plane of $A_1H_1G_1$.

For the tetrahedron $A_1B_1G_1H_1$ with four known vertex coordinates $(x_{A_1}, y_{A_1}, z_{A_1})$, $(x_{B_1}, y_{B_1}, z_{B_1})$, $(x_{G_1}, y_{G_1}, z_{G_1})$, and $(x_{H_1}, y_{H_1}, z_{H_1})$, the volume is calculated by

$$V_{A_1B_1G_1H_1} = \frac{1}{6} \times \begin{vmatrix} 1 & 1 & 1 & 1 \\ x_{A_1} & x_{B_1} & x_{G_1} & x_{H_1} \\ y_{A_1} & y_{B_1} & y_{G_1} & y_{H_1} \\ z_{A_1} & z_{B_1} & z_{G_1} & z_{H_1} \end{vmatrix}$$

$$= \frac{1}{6} \times \begin{vmatrix} x_{B_1} - x_{A_1} & x_{G_1} - x_{A_1} & x_{H_1} - x_{A_1} \\ y_{B_1} - y_{A_1} & y_{G_1} - y_{A_1} & y_{H_1} - y_{A_1} \\ z_{B_1} - z_{A_1} & z_{G_1} - z_{A_1} & z_{H_1} - z_{A_1} \end{vmatrix} \quad (9)$$

In general, the triangular patch is not parallel to the projection plane since the interior surface of the chamber is curved. Therefore, the convex pentahedron is an irregular geometry, and it is difficult to calculate its volume directly. To overcome this problem, the convex pentahedron can be divided into several regular geometric bodies, then the volume of the convex pentahedron is obtained by calculating the sum of the volumes of the regular geometric bodies.

Due to the similarity between the convex pentahedron and the triangular prism in shape, the convex pentahedron can be divided into a triangular prism and the rest geometric part is a rectangular pyramid (shown in Fig. 14(a)). However, the volume calculation of the rectangular pyramid is also complicated. Thus, the rectangular pyramid also needs to be divided and two triangular pyramids (called tetrahedron) are obtained (shown in Fig. 14(b)). The volume of the tetrahedron can be directly calculated under the circumstances that vertex coordinates of the tetrahedron are known.

The final result is that the convex pentahedron is divided into a triangular prism and two tetrahedrons, and the volume calculation of the convex pentahedron is transformed to the volume calculations of a triangular prism and two tetrahedrons. Figure 14(c) is the complete volume segmentation of the convex pentahedron, and $A_1B_1C_1D_1E_1F_1$ is the original convex pentahedron, $A_1H_1G_1D_1E_1F_1$ is the triangular prism, and $A_1B_1C_1G_1$ and $A_1B_1G_1H_1$ are the tetrahedrons.

For a triangle $D_1E_1F_1$ with known vertex coordinates (see Fig. 15), the area of the triangle is calculated by

$$S_{\Delta D_1E_1F_1}$$
$$= \frac{|x_{F_1} \times y_{E_1} + y_{F_1} \times x_{D_1} + x_{E_1} \times y_{D_1} - x_{F_1} \times y_{D_1} - y_{F_1} \times x_{E_1} - y_{E_1} \times x_{D_1}|}{2}$$

$$(7)$$

The volume of triangular prism $A_1H_1G_1D_1E_1F_1$ is calculated by

$$V_{A_1H_1G_1D_1E_1F_1} = S_{\Delta D_1E_1F_1} \times h_{A_1E_1} \quad (8)$$

$$S_{\Delta D_1E_1F_1} = \frac{|x_{F_1} \times y_{E_1} + y_{F_1} \times x_{D_1} + x_{E_1} \times y_{D_1} - x_{F_1} \times y_{D_1} - y_{F_1} \times x_{E_1} - y_{E_1} \times x_{D_1}|}{2}$$

Fig. 15 Area calculation of triangle with three known vertex coordinates

2.3 The Model for Obtaining an Optimized Machining Parameter

2.3.1 Objective Function and Constraints. In order to determine the optimal milling parameter to minimize the volume difference of any two ones of all the chambers, a model based on multi-objective optimization is proposed. The model is developed based on the following three hypotheses: (1) Milling process for the workpiece is face milling, which means that the milling parameter of each chamber is the same. (2) The interior surfaces of the multiple chambers are not machined. (3) The shape of the interior surface of the chamber is similar to a sphere.

The volume variation control of multiple chambers is equivalent to minimizing the volume difference of any two ones of all the chambers. Then, the objective functions are expressed as Eq. (10). For volume variation control of n chambers, the number of the objective functions is $(n(n-1)/2)$

$$\min|(V_i - f_i(h_0)) - (V_j - f_j(h_0))| \quad (i,j = 1, 2, 3, \ldots, n, i < j)$$
$$(10)$$

where V_i and V_j are the volumes of the ith and jth chambers before milling, h_0 is the final milling parameter output by the model, and $f_i(\cdot)$ is the function to calculate the volume of the milled part of the ith chamber.

The volume of each chamber can be calculated with the point cloud according to Sec. 2.2, and this volume is signed as V_i. The ideal milling parameter of the ith chamber is calculated by Eq. (11) if the underside of workpiece for the ith chamber is milled to make its volume equal to the designed volume

$$h_i = F_i(V_i - V_0) \quad (11)$$

where V_i is the volume of the ith chamber before milling, V_0 is the designed volume of the chamber, h_i is the milling parameter of the chamber when milled to the designed volume (V_0), and F_i is the relationship between h_i and ($V_i - V_0$), which is shown in detail in Sec. 2.3.2.

According to the third hypothesis, the milled part of the ith chamber is a part of a sphere, and the cutaway picture of the ith chamber with milled part is shown in Fig. 16. h_0 is the milling parameter to be optimized.

The center O_i and the radius R_i of the sphere can be calculated by LS method when the points on the interior surface of the ith chamber are enough. The distance from the center to the underside of workpiece for the ith chamber before milling is calculated as

$$H_i = \sqrt{R_i^2 - r_i^2} \quad (12)$$

where H_i is the distance between the center of the fitted sphere of the ith chamber and the underside of workpiece for the ith chamber, R_i is the radius of the fitted sphere of the ith chamber, and r_i

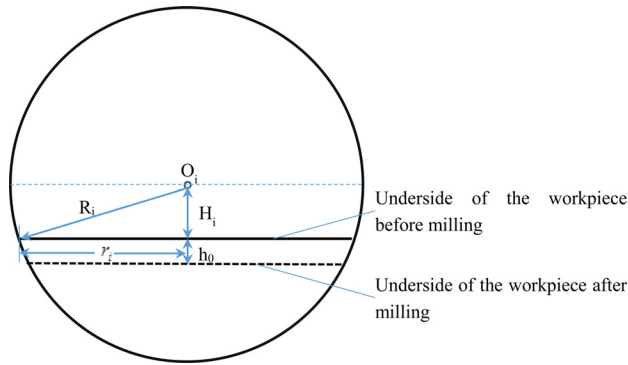**Fig. 16   The cutaway picture of the chamber with milled part**
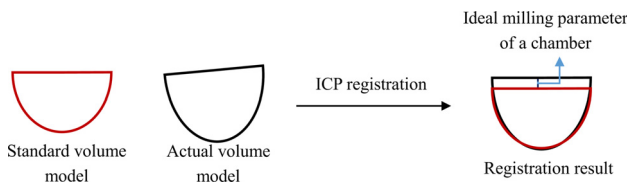

Fig. 17   Calculation of the optimal milling parameter of a single combustion chamber

is the radius of extracted bound from the point cloud of the ith chamber.

The milled part can be regarded as the volume integral of the parallel section area (a circle), and the volume of the milled part is calculated by

$$f_i(h_0) = \int_{H_i}^{H_i+h_0} \pi \times \left(\sqrt{R_i^2 - r^2} \right)^2 dr \qquad (13)$$

where h_0 is the final milling parameter output by the model, and $f_i(h_0)$ is the volume of the milled part of the ith chamber.

Then, the volume of the ith chamber after milling can be calculated by

$$v_i = V_i - f_i(h_0) \qquad (14)$$

The volume of the ith chamber milled according to the milling parameter should satisfy the designed volume and tolerance requirement of the chamber, which is shown as

$$v_i \in [V_0 - v_0, V_0 + v_0] \qquad (15)$$

where v_0 is the variable of designed volume of a single chamber.

The range of the milling parameter is given by

$$h_0 \in [\min(h_i), \max(h_i)] \qquad (16)$$

2.3.2   Calculation of Ideal Milling Parameter of Each Chamber. In order to calculate the ideal milling parameter of each chamber, registration is applied to match the measured point cloud and geometric model of the chamber. In the registration, a rotation matrix and a translation vector are obtained. The ideal milling parameter of each chamber is calculated based on the Z coordinate value of the rotation matrix, and the schematic diagram is shown in Fig. 17.

The registration contains two steps of initial registration and high-accuracy registration. Initial registration is aimed to reduce misplacement of the rotation and translation of the point cloud and thus improves the efficiency and trend of the registration. High-accuracy registration is to minimize the registration error between two-point clouds.

In initial registration, main direction of the legitimate is applied to adjust the reference coordinate systems of the measured point cloud and geometric model to be same. The main direction of the point cloud can be fitted by calculating the feature vector of the point cloud. Take the main direction as a coordinate axis, and two directions perpendicular to the main direction are regarded as the other two coordinate axes, then a three-dimensional coordinate system is established. For two-point clouds to be registered, establish two such coordinate systems and adjust them to be same, and the initial registration of the point cloud is achieved.

In high-accuracy registration, iterative closest point (ICP) algorithm [19] is one of the most widely used algorithms, and the details of ICP algorithm are shown in Appendix A. The procedure of calculating ideal milling depth of each chamber using ICP is included as follows:

Step 1: Determination of initial corresponding point sets. The corresponding point set is determined by directly searching a point of an actual volume model that is closest to a point in standard volume model. The point-to-point search is easy to implement but it cannot satisfy the computational time in terms of huge point cloud. Therefore, k–d tree [20,21] is applied to accelerate the match of point set.

Step 2: Remove of mismatched point sets. In order to remove the mismatched point sets, distance constraint is used to evaluate whether the corresponding point set is reliable. The distances of all the corresponding point sets are calculated and ordered in descending sequence. Then, a number of corresponding point sets in front of the order in descending sequence are regarded as the mismatched point sets and removed from the initial corresponding point sets, which is a substitute for a fixed threshold to remove mismatched point sets.

Step 3: Solution of coordinate transformation. For eventually established corresponding point set, LS method based on unit quaternions [22] is used to iteratively calculate the optimal general coordinate transformation between two-point clouds. In the calculation, the translation vector can be ignored, and the X and Y coordinate values of the rotation matrix can be set as 1 since the purpose of registration in this model is only to obtain the Z coordinate values of the rotation matrix.

Once the procedure is terminated, a rotation matrix is output. Then, the point cloud of the bottom surface of the cylinder head is rotated with the output matrix. The distance between the rotated bottom surface of the cylinder head and the bottom surface of the reference point cloud is the ideal milling parameter of each chamber.

2.4   Model Solution. Particle swarm optimization (PSO) algorithm contains the advantages of efficient global search capability, fast search speed, and simple structure [3,23,24]. However, traditional PSO algorithm cannot be directly applied to solve multi-objective optimization (MOO) problem. The following problems should be solved if PSO algorithm is effectively used for solving MOO problem: (1) How to determine which particle is more preferably between two particles. (2) How to select individual extreme value and global extreme value. (3) How to maintain the uniformity of solution distribution of the algorithm.

In order to overcome the above problems, the multi-objective particle swarm optimization (MOPSO) based on Pareto dominance relationship is applied [25–27]. In the algorithm, a total of three sets are used to save the particle swarm, the nondominated set, and the external set. The relationships of the three sets are shown in Fig. 18.

The particle swarm is the main implementation of the search, and the nondominated set and external set are the main sets that save search results. After initialization of the particle swarm and related parameters, select the nondominated particles from particle swarm and insert them into the nondominated set. Although nondominated set is on behalf of the searched optimal particles in current iteration, the optimal particles searched in previous iterations should be isolated. Therefore, insert the nondominated
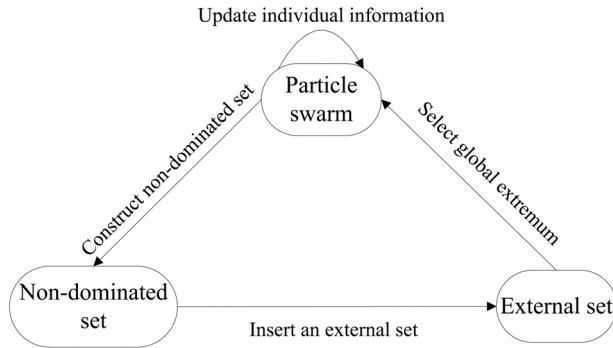
Fig. 18   Multi-objective PSO algorithm

particles obtained in each iteration into the external set. The external set can be regarded as a candidate set of global extreme value. The optimization of particle swarm is guided by the global extreme value to constantly search more optimal solution and then enter the next iteration.

A new procedure of MOPSO algorithm to solve the model for obtaining an optimized milling parameter is shown in Fig. 19.

The details of the procedure of MOPSO algorithm are included as follows. Explanation of some useful notations: p_{best} is the individual optimal position, g_{best} is the global optimal position, x is the current position of a particle and it represents a milling depth, and $F_m(x)$ is the function to calculate the mth volume difference of any two ones of all the chambers with the milling depth x.

Step 1: Initialize the position x_t and velocity λ_t of each particle. Set iterative number, population size, and parameters of the algorithm. The position of each particle is randomly generated in uniform distribution but the range of position values is determined by Eqs. (11) and (16).

Step 2: Calculate the fitness of each particle based on the objective functions of the proposed model. For the first iteration, the
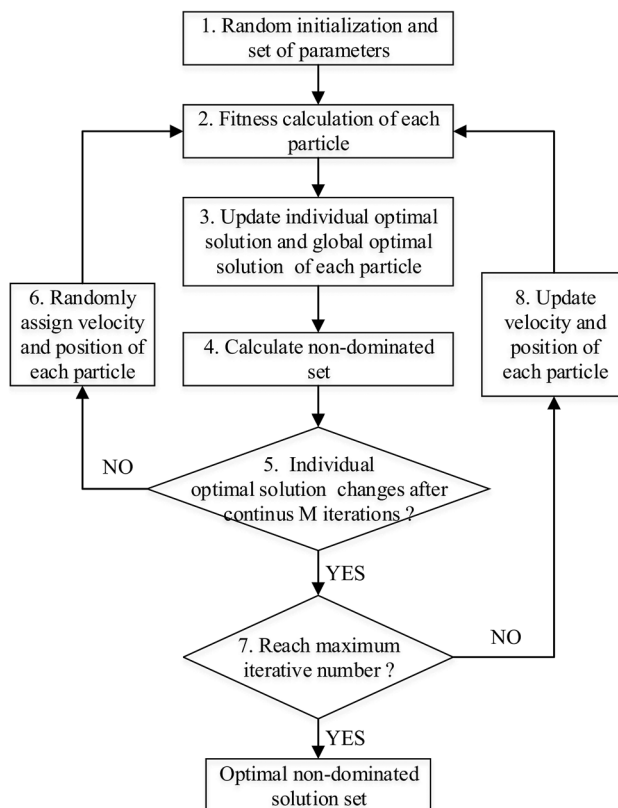

Fig. 19   The procedure of MOPSO algorithm

position of each particle is regarded as the initial p_{best}. The initial nondominated set is selected by the dominated relationship among the particles, and the initial nondominated set is saved as initial external set.

Step 3: Update each particle and guide the particle to search the final global optimal position with the information of global optimal position of current iteration and the historical local optimal position. The update of g_{best} by density distance shown is given as follows.

Sort the particles from the initial external set according to the density distance. Randomly select a particle as g_{best} from the first 20% particles with larger density distances according to the order of density distance. The density distance of each particle is calculated as

$$I(x_i) = \sum_{m=1}^{n} \left| \left[F_m(x_j) - F_m(x_k) \right] \right| \Big/ F_m^{\max} \qquad (17)$$

where x_j and x_k are the closest particles to x_i, and $F_m^{\max}$ is the maximum value of the mth objective function of all the particles.

The update of p_{best} is determined by the dominance relationship between x (current position of the particle) and p_{best} (the best position of current individual particle in its past records). If p_{best} dominates x, then p_{best} remains unchanged. If x dominates p_{best}, x would replace p_{best} as the new p_{best}. If there is no dominance relationship between x and p_{best}, p_{best} remains unchanged or either of x and p_{best} is randomly selected as the new p_{best} with 0.5 probability in traditional algorithm. But in this paper, the selection probability of x and p_{best} is adjusted when there is no dominance relationship between x and p_{best}. For instance, the selection probability of x is set as 0.7, while the selection probability of p_{best} is 0.3. The set of selection probability makes p_{best} in each iteration be different from the last generation, which can prevent the particle from searching the region once searched under the condition of several continuous iterations of the p_{best} without changing.

Step 4: Calculate the nondominated set. The particles are sorted based on the noninferior ordering and the density distance. The number of individuals in nondominated set can be adjusted based on the density distance, which distributes Pareto frontier evenly.

Step 5: Check whether the local optimal value of the particle is enhanced for continuous M iterations. If the local optimal value is not enhanced, go to step 6, otherwise go to step 7.

Step 6: Randomly assign the position and velocity of the particle. Then, go to step 2.

Step 7: Check whether the result satisfies the iteration condition (the maximum iterative number is reached). If the maximum iterative number is not reached, go to step 8. Otherwise, go to step 9.

Step 8: Update the velocity and position of each particle according to the following equations:

$$\lambda_t = \omega \lambda_{t-1} + \alpha_1 \mu_1 (p_{best} - x_{t-1}) + \alpha_2 \mu_2 (g_{best} - x_{t-1}) \qquad (18)$$

$$\lambda_t = \begin{cases} \lambda_{\max}, & \lambda_t > \lambda_{\max} \\ -\lambda_{\max}, & \lambda_t \leq \lambda_{\max} \end{cases} \qquad (19)$$

$$x_t = x_{t-1} + \lambda_t \qquad (20)$$

where ω is the inertia weight, α_1 and α_2 are the acceleration constraints, $\mu_1, \mu_2 \in [0, 1]$ are the random values, and x_t is the current position of the particle that represents the milling parameter.

Step 9: The algorithm terminates and outputs optimal nondominated solution set (the external set), namely, Pareto optimal frontier (see Fig. 20).

The output of the algorithm is a set of nondominated solutions, while there is only a solution that is needed in the proposed model. Therefore, the most optimal solution should be selected from the set of nondominated solutions.

Spacing (SP) is regarded as the index to evaluate the uniformity of the distribution of the Pareto optimal front in the target space. SP is calculated by
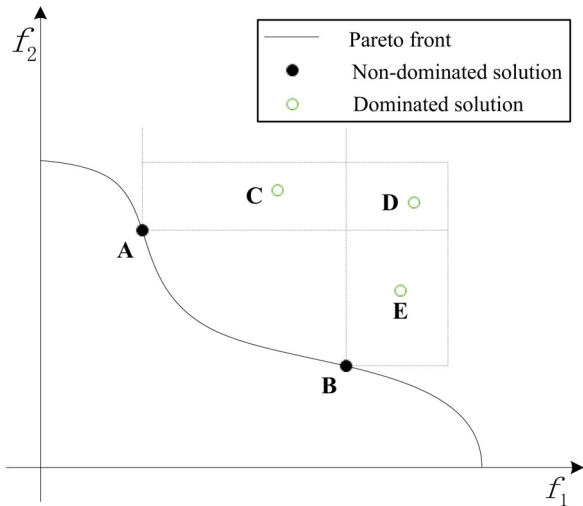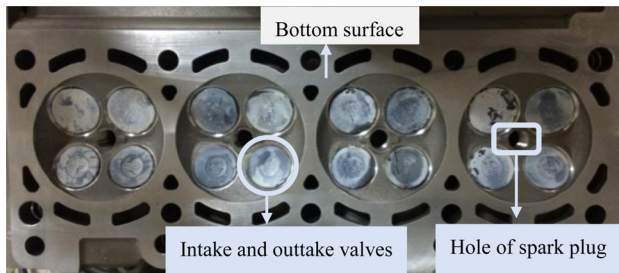
Fig. 20 The diagram of Pareto front
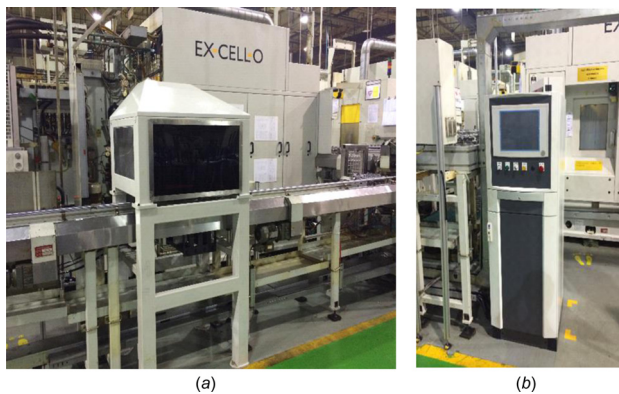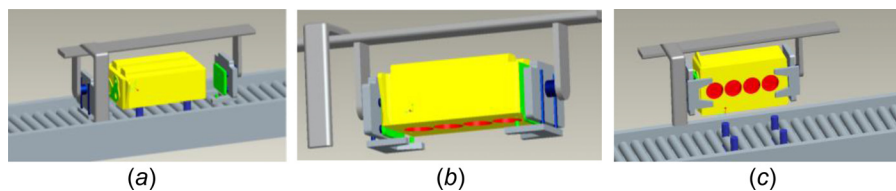
$$SP = \sqrt{\frac{1}{n_0 - 1} \sum_{i=1}^{n_0} (\bar{d} - d_i)^2} \qquad (21)$$

$$\bar{d} = \frac{1}{n_0} \sum_{i=1}^{n_0} d_i \qquad (22)$$

where n_0 is the number of Pareto optimal solutions, and d_i represents the minimum value of the Euclidean distance between the target point of the ith Pareto optimal solution and all the points of the real Pareto front of the problem.

The number of the objective function is m, and d_i is calculated as

$$d_i = \min_j \left((F_1(x_i) - F_1(x_j))^2 + (F_2(x_i) - F_2(x_j))^2 \right.$$
$$\left. + \cdots + (F_m(x_i) - F_m(x_j))^2 \right)^{1/2} \qquad (23)$$

where $j \neq i, j = 1, 2, \ldots, m$.

If $SP = 0$, it indicates that the Pareto optimal front is evenly distributed. In order to choose the best solution from the Pareto optimal front, the solution with the least SP value is regarded as the final solution of the proposed model.

3 Case Study

3.1 Machining Process Description. In this case, the cylinder heads of B12 serial engine with four combustion chambers (see Fig. 21) are used to validate the performance of the proposed approach on volume variation control of multiple chambers. Before the measurement, the intake and out-take valves are put into the combustion chambers and the hole of the spark plug has been reamed.

The volumes of combustion chambers of B12 engine cylinder head are measured by an online HDM measurement machine using laser triangulation metrology [28,29]. Figure 22 is the online measurement equipment. Figure 23 exhibits the measurement process. Figure 24 shows the actual operation of the online measurement equipment.

The field view of the HDM system is within 75×56 mm^2, and the depth of field view is 15 mm. Accuracy in X (translation direction) is $\pm 1\,\mu$m. Accuracy in Y (direction of line laser) is $\pm 10\,\mu$m. Accuracy in Z is $\pm 20\,\mu$m. Resolution of the system is 0.02 mm^3. Repeatability is 0.02 ml.

In this case, the moving speed of the guide rail is set at 10 mm/s, and the acquisition frame rate of the three-dimensional measurement sensors is 110 f/s. The scan time of the cylinder head depends on the length of the cylinder head and speed of guide rail. The scan time of the cylinder head is 32 s. Besides, the measurement time also includes time of grab (20 s), drop (15 s), and leave (10 s). Therefore, the total measurement time is 77 s, which is less than the cycle time of manufacturing a cylinder head 87.5 s, and the online measurement can be easily implemented. The measurement time of the system is adjustable, and faster measurement can be achieved by increasing the speed of guide rail and acquisition speed of the system. 2000×1280 is the number of points that are

Fig. 21 Cylinder head of B12 engine with four combustion chambers

Fig. 22 Online measurement equipment based on HDM system: (a) measurement component and (b) industrial personal computer

Fig. 23 The measurement process: (a) locate, (b) clamp, and (c) flip over
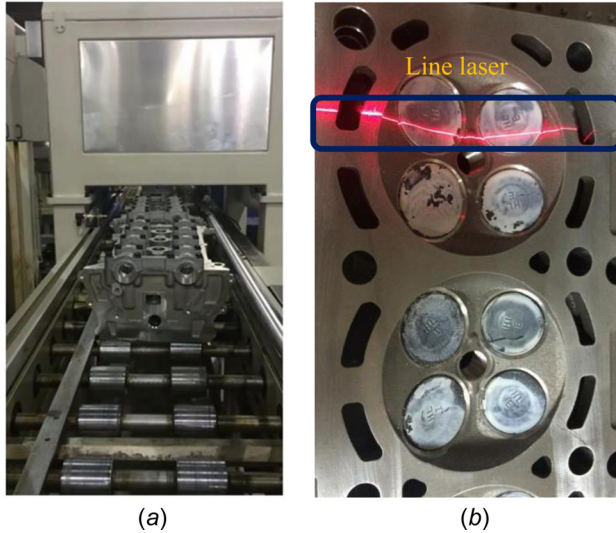
Fig. 24 Actual operation of the online measurement equipment: (*a*) online measurement and (*b*) an example of measurement

collected from a cylinder head by the HDM system. It includes the bottom surface and all the chambers of a cylinder head. There are 2000 points on a laser line, and the total measurement contains 1280 laser lines. Once the point cloud of the combustion chambers

is obtained, the volume of these combustion chambers can be calculated by the proposed point cloud processing algorithm and volume calculation method.

The cylinder head milling operations influencing the volumes of combustion chambers are shown in Fig. 25. F1000 is the underside of the cylinder head and F2000 is the top surface of the cylinder head, and OP10, OP20, OP80, and OP140 are the operation sequence numbers. Among the four operations, the measurement of the cylinder head is conducted after OP80. The optimized finish-milling parameter is input into the computer numerical control (CNC) machine on OP140, and the control of volume variation of the four combustion chambers is implemented on OP140. The CNC machine to mill the cylinder head is EX-CELL-O XS211. Ten cylinder heads are measured and machined in this case.

3.2 Results and Analysis

3.2.1 Datum Transformation. The point cloud of the cylinder head measured by the online measurement machine is shown in Fig. 26(*a*). It can be seen that the underside of the cylinder head mapped by the point cloud is inclined, which means that *Z* coordinates of points on the underside of the cylinder head are not approximately zero. Therefore, datum transformation of the measured point cloud is necessary. The point cloud after datum transformation is shown in Fig. 26(*b*). The filtering result of the point cloud is shown in Fig. 27.

3.2.2 Volume Calculation. The reconstruction result of curved surface of combustion chambers is shown in Fig. 28. It can be seen from Fig. 28(*a*) that the hole of the spark plug has been
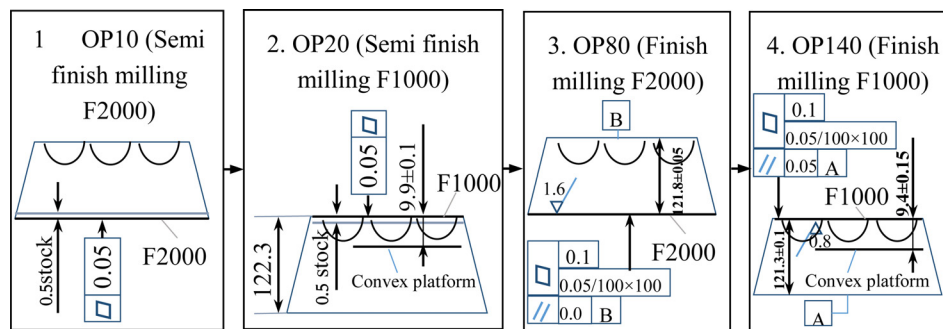

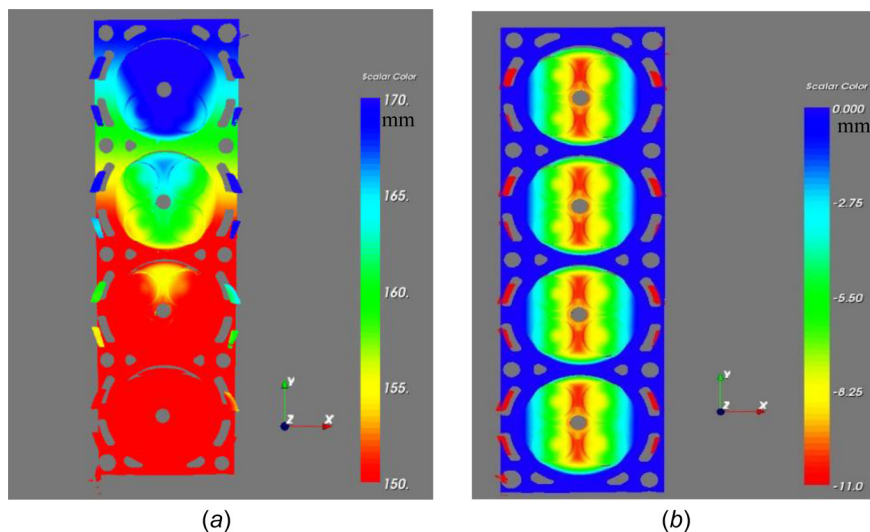**Fig. 25 Process of machining combustion chambers of cylinder head**

Fig. 26 Point cloud before and after datum transformation: (*a*) point cloud measured by HDM and (*b*) point cloud transformed by RANSAC
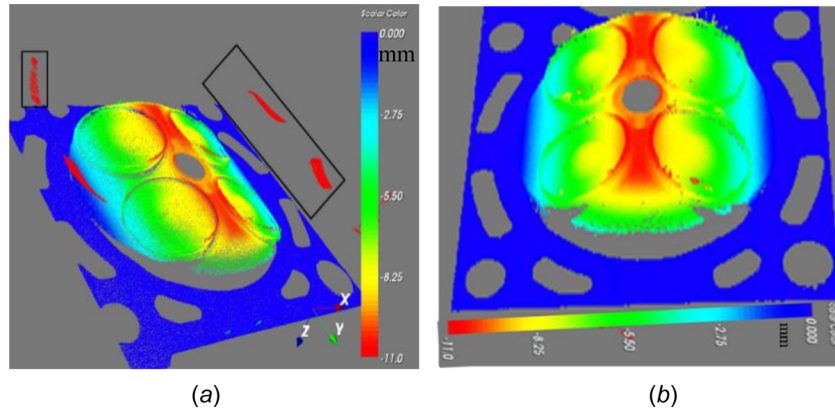
Fig. 27 Point cloud before and after filtering: (*a*) point cloud before filtering and (*b*) point cloud after filtering
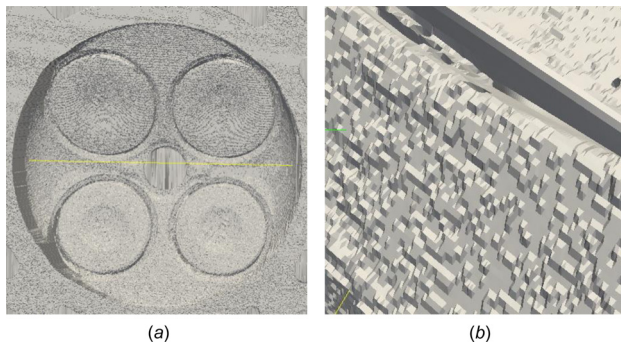

Fig. 28 Cylinder head combustion chamber surfaces after reconstruction: (*a*) reconstruction result of a combustion chamber and (*b*) local amplification of the reconstructed surface of combustion chambers

completely interpolated. Meshless algorithm can effectively carry out the triangulation of the point cloud since the local grid of cylinder head combustion chamber (shown in Fig. 28(*b*)) is relatively smooth and an obvious grid shape is presented.

The boundary extraction includes two steps: The first step is to determine the number of initial and terminal rows according to the average *Z* coordinate value of each row. An example of a combustion chamber is shown in Fig. 29, and the initial and terminal rows are 17 and 140, respectively.

The second step is to determine the number of initial and terminal points of each row determined in the first step according to *Z* coordinate value of each row. Figure 30 shows the point numbers of the initial and terminal points of a determined row.
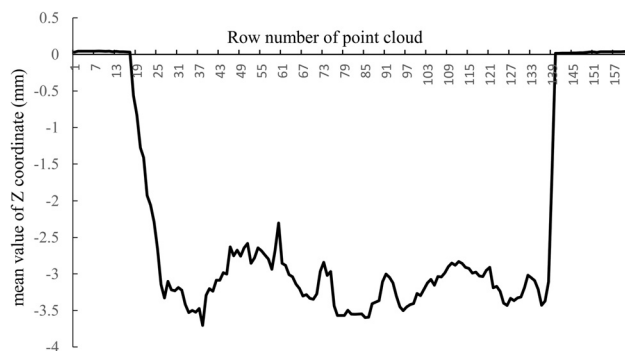

Fig. 29 Statistical averages of *Z* coordinates of each point cloud row
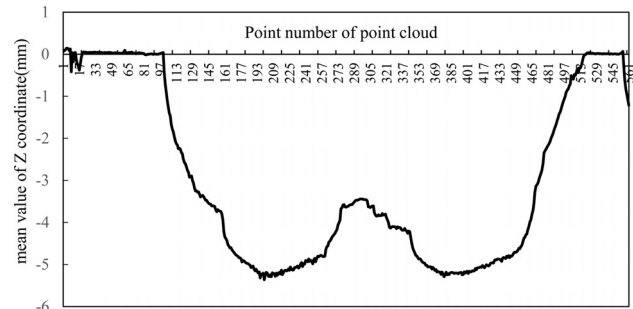

Fig. 30 Efficient point cloud boundary extraction

Repeat the process of the second step from the 17th row to the 140th row, and the efficient boundary point set of cylinder head combustion chamber can be obtained (see Fig. 31). Then, the parameters of the boundary can be obtained by the fitting algorithm of LS.

With the projection algorithm calculating the volumes of multiple chambers before milling, the volumes of the four combustion chambers (take a cylinder head for example) are 26.03 ml, 26.26 ml, 26.34 ml, and 26.26 ml, respectively.

3.2.3 The Model for Obtaining an Optimized Milling Parameter. For the cylinder head with four combustion chambers, the six objective functions are expressed as

$$\text{Min}\left(|v_1 - v_2|, |v_1 - v_3|, |v_1 - v_4|, |v_2 - v_3|, |v_2 - v_4|, |v_3 - v_4|\right) \tag{24}$$

The volumes of the four combustion chambers before OP140 workstation are expressed as

$$V_1 = 26.03, V_2 = 26.26, V_3 = 26.34, V_4 = 26.26 \tag{25}$$

According to Sec. 2.2.2, boundary radii of the four combustion chambers are 35.0378 mm, 34.8576 mm, 35.0829 mm, and 35.0445 mm, respectively. The fitted sphere radii of the four combustion chambers are 60.1581 mm, 61.7508 mm, 60.5026 mm, and 62.8705 mm. The distances from the center to the underside of the workpiece for each chamber before milling are

$$H_1 = 48.9014, H_2 = 50.9716, H_3 = 49.2925, H_4 = 52.1975 \tag{26}$$

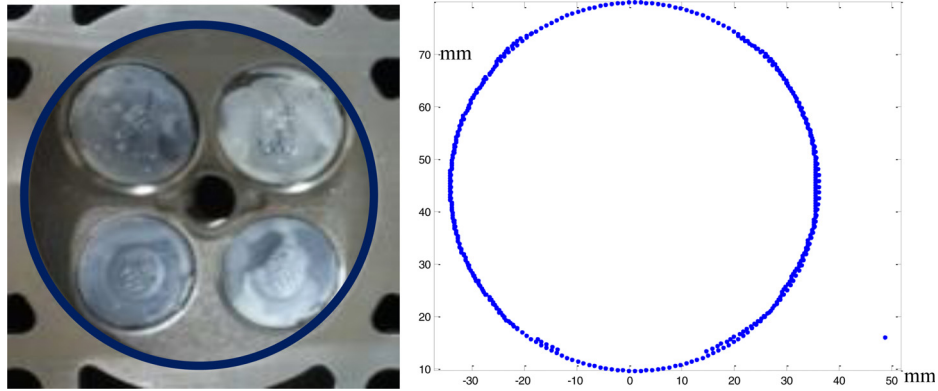Then, the volumes of the milled parts of the four combustion chambers are

Fig. 31 Cylinder head combustion chamber boundary

Table 1 Optimal milling parameters (h_0), volume of each cylinder head chamber, and volume differences of any two ones of all the chambers after milling

Volume (ml)	1	2	3	4	5	6	7	8	9	10
h_0 (mm)	0.534	0.539	0.552	0.511	0.538	0.541	0.538	0.539	0.468	0.489
v_1	24.36	24.35	24.24	24.49	24.31	24.28	24.29	24.37	24.24	24.26
v_2	24.45	24.53	24.39	24.65	24.55	24.56	24.43	24.46	24.44	24.46
v_3	24.41	24.31	24.38	24.2	24.35	24.55	24.45	24.43	24.53	24.45
v_4	24.22	24.32	24.17	24.19	24.30	24.20	24.28	24.26	24.48	24.38
$|v_1 - v_2|$	0.09	0.18	0.15	0.16	0.24	0.28	0.14	0.09	0.20	0.20
$|v_1 - v_3|$	0.05	0.04	0.14	0.29	0.04	0.27	0.16	0.06	0.29	0.19
$|v_1 - v_4|$	0.14	0.03	0.07	0.30	0.01	0.08	0.01	0.11	0.24	0.12
$|v_2 - v_3|$	0.04	0.22	0.01	0.45	0.2	0.01	0.02	0.03	0.09	0.01
$|v_2 - v_4|$	0.23	0.21	0.22	0.46	0.25	0.36	0.15	0.20	0.04	0.08
$|v_3 - v_4|$	0.19	0.01	0.21	0.01	0.05	0.35	0.17	0.17	0.05	0.07

$$f_1(h_0) = \int_{48.9014}^{48.9014+h_0} \pi \times \left(\sqrt{61.1581^2 - r^2} \right)^2 dr$$

$$f_2(h_0) = \int_{50.9716}^{50.9716+h_0} \pi \times \left(\sqrt{61.7508^2 - r^2} \right)^2 dr$$

$$f_3(h_0) = \int_{49.2925}^{49.2925+h_0} \pi \times \left(\sqrt{60.5026^2 - r^2} \right)^2 dr \qquad (27)$$

$$f_4(h_0) = \int_{52.1975}^{52.1975+h_0} \pi \times \left(\sqrt{62.8705^2 - r^2} \right)^2 dr$$

The volumes of the four combustion chambers after milling are calculated by

$$
\begin{aligned}
v_1 &= V_1 - f_1(h_0) \\
v_2 &= V_2 - f_2(h_0) \\
v_3 &= V_3 - f_3(h_0) \\
v_4 &= V_4 - f_4(h_0)
\end{aligned}
\qquad (28)
$$

The designed volume is 24.4 ml and tolerance requirement is ± 0.4 ml, then the constraint of Eq. (16) is replaced by

$$24.4 - 0.4 \leq v_1, v_2, v_3, v_4 \leq 24.4 + 0.4 \qquad (29)$$

With the ICP algorithm calculating the ideal milling parameters of the four combustion chambers, the four ideal milling parameters are expressed as

$$h_1 = 0.426\,\text{mm}, h_2 = 0.488\,\text{mm}, h_3 = 0.509\,\text{mm}, h_4 = 0.488\,\text{mm} \qquad (30)$$

The range of the optimal milling parameter is [min (h_1, h_2, h_3, h_4), max (h_1, h_2, h_3, h_4)], which is expressed as

$$0.426 \leq h_0 \leq 0.509 \qquad (31)$$

3.2.4 Model Solution. With MOPSO algorithm solving the model, the optimal milling parameter of the four combustion chambers is 0.468 mm, and the volumes of the four combustion chambers after milling with the optimal parameter are 24.24 ml, 24.44 ml, 24.53 ml, and 24.48 ml, respectively. In this case, other nine cylinder heads are milled with the parameter optimized by the proposed approach. The optimal milling parameters (h_0), volumes of the ten cylinder heads, and volume differences of any two ones of all the chambers of the ten cylinder heads after milling are shown in Table 1. The volumes of the combustion chambers of the ten cylinder heads and the volume differences of any two ones of all the chambers of the ten cylinder heads before milling are shown in Table 2.

For comparison, the volume differences of any two ones of all the chambers of the cylinder heads before and after milling are shown in Appendix B. In order to evaluate the volume variation of cylinder head combustion chambers reasonably, reducing the maximum difference of any two ones of all the chambers of a cylinder head can be considered as an indicator of improvement by the proposed approach. The comparison of the maximum volume difference between two chambers of the ten cylinder heads is shown in Fig. 32.

Table 3 shows the control performance of maximum volume variation of each cylinder head after milling. The ratio of reducing the maximum volume difference should be calculated by maximum variation reduction ratio (MVRR) = ($V_{\text{before milling}} - V_{\text{after milling}}$)/0.8, where $V_{\text{before milling}}$ is the

Table 2 Volumes of each cylinder head and volume differences of any two ones of all the chambers of each cylinder head before milling

| Volume (ml)	1	2	3	4	5	6	7	8	9	10
V_1	26.48	26.39	26.37	26.44	26.42	26.36	26.39	26.43	26.03	26.16
V_2	26.55	26.59	26.56	26.6	26.65	26.64	26.53	26.54	26.26	26.37
V_3	26.49	26.38	26.56	26.13	26.41	26.59	26.56	26.51	26.34	26.38
V_4	26.28	26.39	26.34	26.1	26.32	26.21	26.39	26.35	26.26	26.3
$|V_1 - V_2|$	0.07	0.20	0.19	0.16	0.23	0.28	0.14	0.11	0.23	0.21
$|V_1 - V_3|$	0.01	0.01	0.19	0.31	0.01	0.23	0.17	0.08	0.31	0.22
$|V_1 - V_4|$	0.20	0.01	0.03	0.34	0.10	0.15	0.00	0.08	0.23	0.14
$|V_2 - V_3|$	0.06	0.21	0.00	0.47	0.24	0.05	0.03	0.03	0.08	0.01
$|V_2 - V_4|$	0.27	0.20	0.22	0.50	0.33	0.43	0.14	0.19	0.00	0.07
$|V_3 - V_4|$	0.21	0.01	0.22	0.03	0.09	0.38	0.17	0.16	0.08	0.08
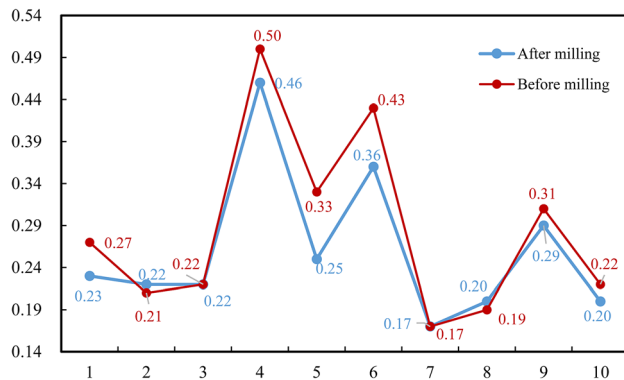
Fig. 32 Maximum volume variation of combustion chambers of each cylinder head before and after milling

maximum volume variation of each cylinder before milling, $V_{\text{after milling}}$ is the maximum volume variation of each cylinder after milling, and 0.8 is the sum of designed tolerance requirement (± 0.4 ml). The decrease ratio (DR) after milling is calculated by $\text{DR} = (V_{\text{before milling}} - V_{\text{after milling}})/V_{\text{before milling}}$.

It can be seen from Fig. 32 that the proposed approach exhibits good performance on decreasing maximum volume variation of combustion chambers. Table 3 shows the explicit and notable decrease of maximum volume variation of combustion chambers of each cylinder head before and after milling. The maximum decrease is 24.24% and other positive decreases are very large, which can effectively enhance the compression ratio consistency. It also can be seen that the negative decreases occur when the maximum volume variation of combustion chambers before milling is small. The reason is that the cylinder head with small volume differences of any two ones of all the chambers (the maximum volume variation is less than 0.22 ml) is more sensitive

to the machining errors, such as the machine tools accuracy and positioning accuracy. Although there exist several negative and zero decreases of the maximum volume variation by the proposed approach, most of the decreases are positive and values of positive decreases are larger than the values of negative decreases.

In order to better certify the performance of the proposed approach, the normal production process is also conducted on the ten cylinder heads. In the normal production process of OP140, the milling parameter is 0.5 mm and the parameter remains unchanged. Every cylinder head is milled twice with 0.5 mm (nonoptimal strategy) and the optimal parameter h_0 (optimal strategy). The milling sequence depends on the values of 0.5 and h_0. For instance, if $0.5 < h_0$, the cylinder head is milled with 0.5 mm and measurement of the chambers is conducted. Then, cylinder head is milled with $(h_0 - 0.5)$ mm (optimal strategy), and measurement of the chambers is conducted again. Table 4 shows the volumes of each cylinder head chamber and volume differences of any two ones of all the chambers of each cylinder head after milling with nonoptimal strategy.

Since the milling process is on the same cylinder head, the volumes of chambers before milling are the same with Table 2. Control performance of maximum volume variation of combustion chambers of each cylinder head before and after milling with nonoptimal strategy is shown in Table 5.

The comparison of volume variation control performance of optimal strategy and nonoptimal strategy is shown in Table 6 and Figs. 33 and 34.

It can be seen from Table 6 that the average DR of optimal strategy is 6.89%, which is 4.72% higher than the nonoptimal strategy (2.17%). The average MVRR of the optimal strategy is also 1.88% higher than the nonoptimal strategy. Besides, Figs. 33 and 34 show that the optimal strategy exhibits good performance on decreasing maximum volume variation of combustion chambers and outperforms the nonoptimal strategy. Since each cylinder head is milled twice, there exist processing errors (repeat positioning and clamping errors), which may influence the volume

Table 3 Control performance of maximum volume variation of each cylinder head after milling with the proposed approach

		$V_{\text{before milling}}$	$V_{\text{after milling}}$	DR (%)	MVRR (%)
Maximum volume variation (ml)	1	0.27	0.23	14.81	5.00
	2	0.21	0.22	−4.76	−1.25
	3	0.22	0.22	0	0
	4	0.5	0.46	8.00	5.00
	5	0.33	0.25	24.24	10.00
	6	0.43	0.36	16.28	8.75
	7	0.17	0.17	0	0
	8	0.19	0.2	−5.26	−1.25
	9	0.31	0.29	6.45	2.50
	10	0.22	0.2	9.09	2.50
	Average	0.285	0.26	6.89	3.13

Table 4 Volume of each cylinder head chamber and volume differences of any two ones of all the chambers after milling with non-optimal strategy

Number	1	2	3	4	5	6	7	8	9	10
v_1	24.42	24.43	24.33	24.52	24.39	24.35	24.36	24.42	24.16	24.24
v_2	24.53	24.60	24.47	24.68	24.64	24.66	24.52	24.52	24.36	24.45
v_3	24.48	24.38	24.47	24.22	24.42	24.63	24.53	24.50	24.47	24.43
v_4	24.27	24.4	24.26	24.20	24.35	24.27	24.34	24.33	24.41	24.36
$|v_1 - v_2|$	0.11	0.17	0.14	0.16	0.25	0.31	0.16	0.10	0.20	0.21
$|v_1 - v_3|$	0.06	0.05	0.14	0.30	0.03	0.28	0.17	0.08	0.31	0.19
$|v_1 - v_4|$	0.15	0.03	0.07	0.32	0.04	0.08	0.02	0.09	0.25	0.12
$|v_2 - v_3|$	0.05	0.22	0.00	0.46	0.22	0.03	0.01	0.02	0.11	0.02
$|v_2 - v_4|$	0.26	0.20	0.21	0.48	0.29	0.39	0.18	0.19	0.05	0.09
$|v_3 - v_4|$	0.21	0.02	0.21	0.02	0.07	0.36	0.19	0.17	0.06	0.07

Table 5 Control performance of maximum volume variation of each cylinder head before and after milling with nonoptimal strategy

		$V_{\text{before milling}}$	$V_{\text{after milling}}$	DR (%)	MVRR (%)
Maximum volume variation (ml)	1	0.27	0.26	3.70	1.25
	2	0.21	0.22	−4.76	−1.25
	3	0.22	0.21	4.55	1.25
	4	0.5	0.48	4.00	2.50
	5	0.33	0.29	12.12	5.00
	6	0.43	0.39	9.30	5.00
	7	0.17	0.19	−11.77	−2.50
	8	0.19	0.19	0	0
	9	0.31	0.31	0	0
	10	0.22	0.21	4.55	1.25
	Average	0.285	0.275	2.17	1.25

Table 6 Comparison of volume variation control performance of optimal strategy and nonoptimal strategy

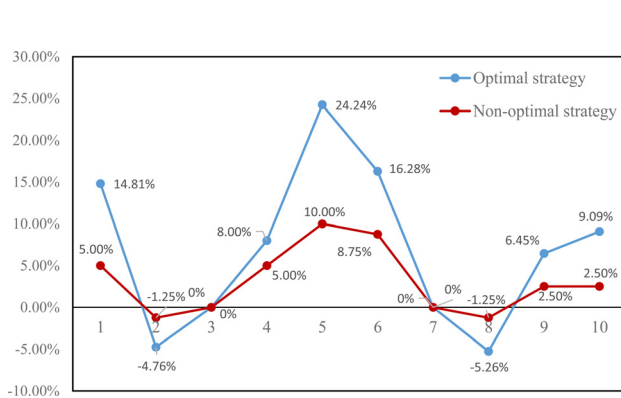|	DR		MVRR	
	Optimal strategy (%)	Nonoptimal strategy (%)	Optimal strategy (%)	Nonoptimal strategy (%)
1	14.81	3.70	5.00	1.25
2	−4.76	−4.76	−1.25	−1.25
3	0	4.55	0	1.25
4	8.00	4.00	5.00	2.50
5	24.24	12.12	10.00	5.00
6	16.28	9.30	8.75	5.00
7	0	−11.77	0	−2.50
8	−5.26	0	−1.25	0
9	6.45	0	2.50	0
10	9.09	4.55	2.50	1.25
Average	6.89	2.17	3.13	1.25

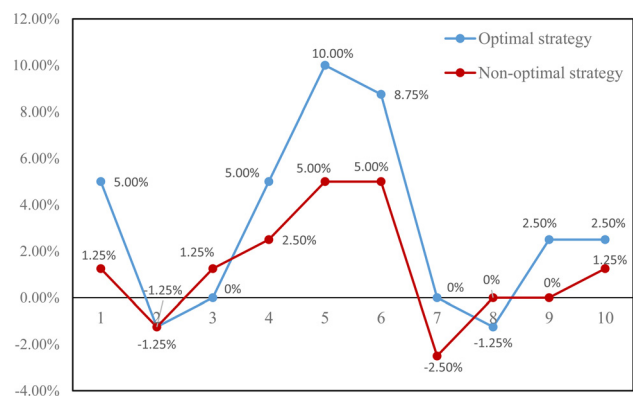Fig. 33 Comparison of the DR of optimal strategy and nonoptimal strategy

Fig. 34 Comparison of the MVRR of optimal strategy and non-optimal strategy
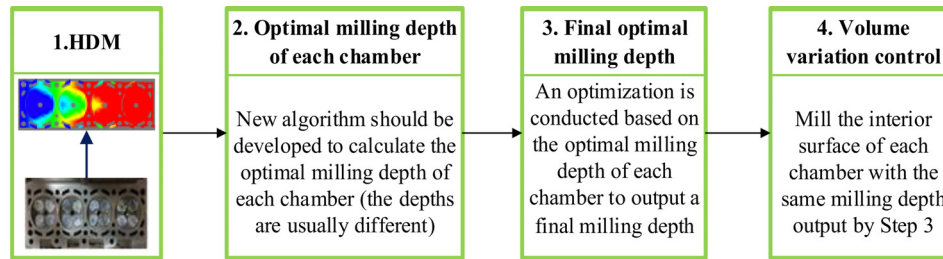
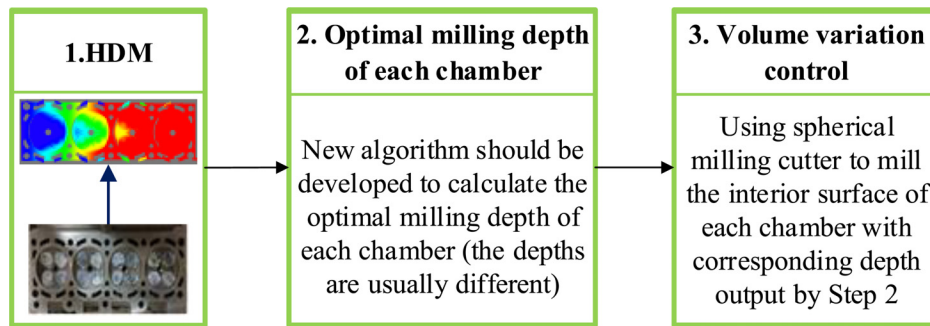**Fig. 35 Procedure of milling interior surfaces with a milling depth**

Fig. 36 Procedure of milling interior surfaces with *n* different milling depths

variation control performance of the optimal strategy. Although there are several worse decreases of the maximum volume variation by the optimal strategy, the total performance is better than the nonoptimal strategy.

4 Conclusions

This paper has developed a systematic approach for online minimizing volume difference of multiple chambers in machining processes based on HDM, which consists of datum transformation, volume calculation, optimization model, and model solution. RANSAC algorithm is used to transform the datum of the HDM point cloud for data preprocessing. The projection method and the proposed boundary extraction method are used to calculate the volumes of the multiple chambers before milling. A model aimed at optimizing the milling parameter is proposed to control volume variation of multiple chambers, and MOPSO algorithm is explored to solve the model. A case study of ten cylinder heads with four combustion chambers is conducted to evaluate the control performance of volume variation. The results demonstrate that the proposed approach can decrease the maximum volume variation of multiple chambers (decrease ratio ranges from 6.45% to 24.24% and maximum variation reduction ratio ranges from 2.50% to 10.00%) and outperforms the normal production process (nonoptimal strategy). In summary, the proposed approach can be well applied online for controlling volume variation of multiple chambers.

The proposed method is applicable to minimizing volume difference of multiple chambers of inline engine, but cannot be directly used in V-type and W-type engines. For future work, control of volume difference of multiple chambers can be extended in three aspects.

(1) Spatial correlation of three-dimensional point cloud of multiple chambers can be applied to identify the mould failure modes of multichamber workpiece. Then, the mould of multichamber workpiece can be better maintained and casts blank workpieces with less volume variation.
(2) New machining technologies (i.e., machining the interior surfaces of the chambers) can be adopted. There are two options for controlling the volume variation of the multiple chambers by milling the interior surfaces of the chambers.

The first option is shown in Fig. 35. Since the milling depths of the *n* chambers are the same, the control performance of volume variation is the same as the proposed approach.

The second option is shown in Fig. 36. In this way, the milling depths of the *n* chambers are different, which is possible to eliminate the volume variation of multiple chambers. But it is quite difficult to dynamically adjust the milling depth of each combustion chamber. For the second option, the new methodology needs to be developed.

(3) Further improvement is possible by using the software for the analysis of the alleged data and automated creation of a program for CNC machine.

Appendix A

In high-accuracy registration, ICP is one of the most widely used algorithms. Assume that a source point cloud $\mathbf{P}$ is registered to be in best alignment with a reference point cloud χ. The aim of ICP is to find the rigid body transformation, rotation matrix $\boldsymbol{q}_R$, and translation vector $\mathbf{q_T}$ that aligns the source with the reference by minimizing the distance

$$E(\boldsymbol{q}_R, \mathbf{q_T}) = \frac{1}{N_P} \sum_{k=1}^{N_P} \| \chi_k - (\boldsymbol{q}_R p_k + \mathbf{q_T}) \|^2 \qquad (A1)$$

where N_P is the point number of point cloud $\boldsymbol{P}$, $\chi_k \in \chi$, $p_k \in \boldsymbol{P}$.

The center of mass μ_P of point cloud $\mathbf{P}$ and the center of mass μ_χ of point cloud χ are calculated as
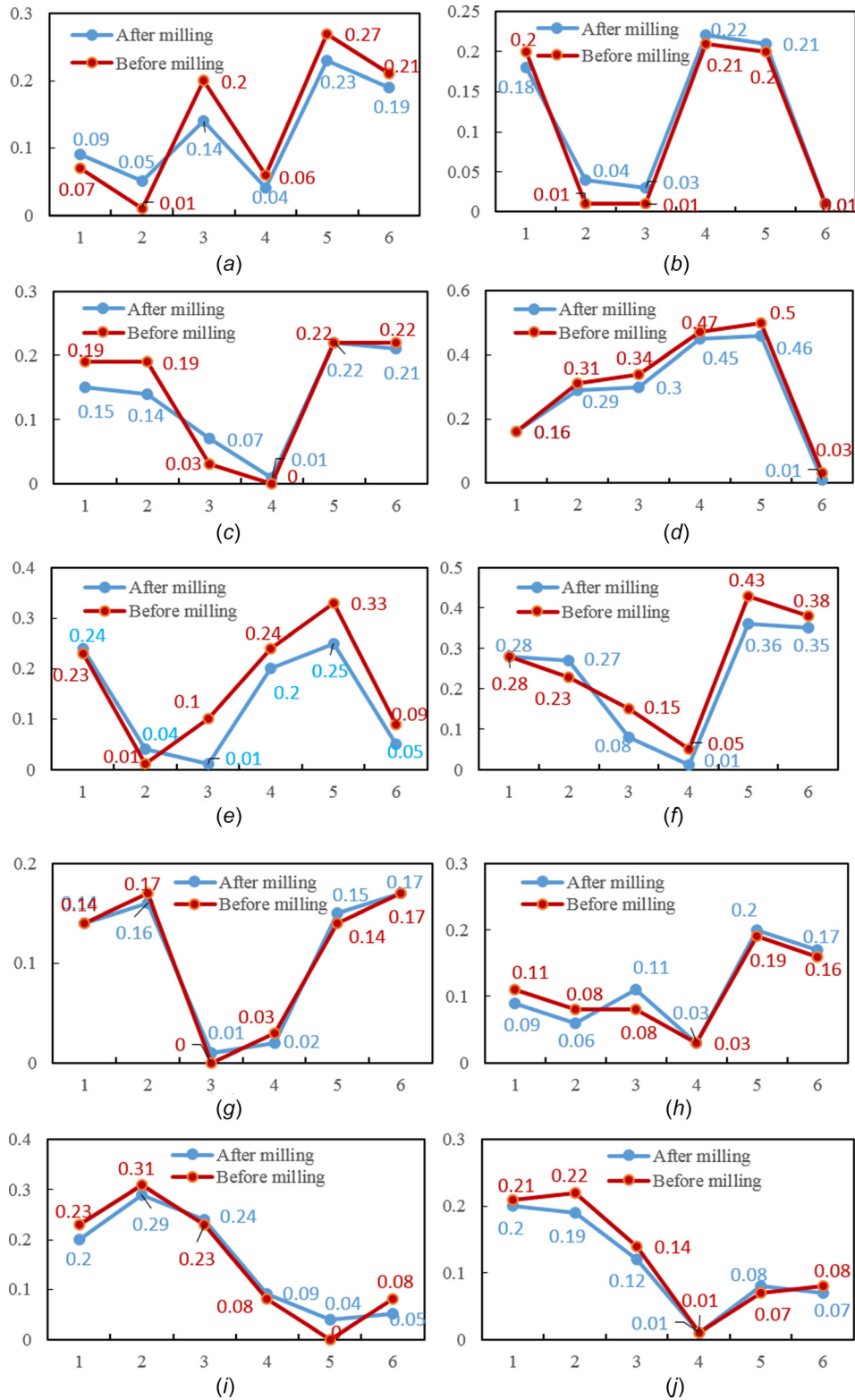
Fig. 37 Comparison of volume variation of combustion chambers of each cylinder head before and after milling: (*a*) comparison of first cylinder head, (*b*) comparison of second cylinder head, (*c*) comparison of third cylinder head, (*d*) comparison of fourth cylinder head, (*e*) comparison of fifth cylinder head, (*f*) comparison of sixth cylinder head, (*g*) comparison of seventh cylinder head, (*h*) comparison of eighth cylinder head, (*i*) comparison of ninth cylinder head, and (*j*) comparison of tenth cylinder head

$$\mu_P = \frac{1}{N_P}\sum_{i=1}^{N_P} p_i, \quad \mu_\chi = \frac{1}{N_X}\sum_{i=1}^{N_\chi} \chi_i \qquad (A2)$$

where N_χ is the point number of point cloud $\boldsymbol{\chi}$.

The cross-covariance matrix of the point clouds $\boldsymbol{P}$ and $\boldsymbol{\chi}$ is calculated as

$$\sum_{\mathbf{P},\boldsymbol{\chi}} = \frac{1}{N_P}\sum_{i=1}^{N_P}\left[(p_i - \mu_P)(\chi_i - \mu_\chi)^{\mathrm{T}}\right] = \frac{1}{N_P}\sum_{i=1}^{N_P}\left[p_i\chi_i^{\mathrm{T}}\right] - \mu_P\mu_\chi^{\mathrm{T}}$$

$$(A3)$$

Then, a symmetric 4×4 matrix is formed based on the cross-covariance matrix $\sum_{\mathbf{P},\boldsymbol{\chi}}$

$$Q\left(\sum_{\mathbf{P},\boldsymbol{\chi}}\right) = \begin{bmatrix} \mathrm{tr}\left(\sum_{\mathbf{P},\boldsymbol{\chi}}\right) & \Delta^{\mathrm{T}} \\ \Delta & \sum_{P,\chi} + \sum_{\mathbf{P},\boldsymbol{\chi}}^{\mathrm{T}} - \mathrm{tr}\left(\sum_{\mathbf{P},\boldsymbol{\chi}}\right)\boldsymbol{I}_3 \end{bmatrix} \qquad (A4)$$

where $\mathrm{tr}\left(\sum_{P,\chi}\right)$ is the trace of matrix $\sum_{P,\chi}$, $\Delta = [A_{23}\ A_{31}\ A_{12}]^{\mathrm{T}}$ is a column vector, $\mathbf{A}_{\mathbf{i},\mathbf{j}} = \left(\sum_{P,X} - \sum_{P,X}^{\mathrm{T}}\right)_{i,j}$, and $\boldsymbol{I}_3$ is the 3×3 identity matrix.

Calculate the eigenvalues and eigenvectors of matrix $\mathbf{Q}\left(\sum_{\mathbf{P},\boldsymbol{\chi}}\right)$, the eigenvector $([q_0\ q_1\ q_2\ q_3]^{\mathrm{T}}, \ q_0 > 0$, and $q_0^2 + q_1^2 + q_2^2 + q_3^2 = 1)$ corresponding to the maximum eigenvalue is regarded as the optimal rotation. The rotation matrix $\mathbf{q_R}$ is calculated as

$$\boldsymbol{q}_R = \begin{bmatrix} q_0^2 + q_1^2 - q_2^2 - q_3^2 & 2(q_1q_2 - q_0q_3) & 2(q_1q_3 + q_0q_2) \\ 2(q_1q_2 + q_0q_3) & q_0^2 - q_1^2 + q_2^2 - q_3^2 & 2(q_2q_3 - q_0q_1) \\ 2(q_1q_3 - q_0q_2) & 2(q_2q_3 + q_0q_1) & q_0^2 - q_1^2 - q_2^2 + q_3^2 \end{bmatrix}$$

$$(A5)$$

The best translation vector $\mathbf{q_T}$ is calculated as

$$\mathbf{q_T} = \mu_X - \boldsymbol{q}_R\mu_P \qquad (A6)$$

Appendix B

For comparison, the volume differences of any two ones of all the chambers of the ten cylinder heads before and after milling are shown in Fig. 37.

References

[1] Coherix, 2010, "Introducing the Latest in High-Definition, Non-Contact Metrology Shapix 1500 Series," Coherix, Ann Arbor, MI, http://www.coherix.com
[2] Du, S., Liu, C., and Huang, D., 2015, "A Shearlet-Based Separation Method of 3D Engineering Surface Using High Definition Metrology," Precis. Eng., 40, pp. 55–73.
[3] Du, S., Liu, C., and Xi, L., 2015, "A Selective Multiclass Support Vector Machine Ensemble Classifier for Engineering Surface Classification Using High Definition Metrology," ASME J. Manuf. Sci. Eng., 137(1), p. 011003.
[4] Du, S. C., Huang, D. L., and Wang, H., 2015, "An Adaptive Support Vector Machine-Based Workpiece Surface Classification System Using High-Definition Metrology," IEEE Trans. Instrum. Meas., 64(10), pp. 2590–2604.
[5] Du, S., and Fei, L., 2016, "Co-Kriging Method for Form Error Estimation Incorporating Condition Variable Measurements," ASME J. Manuf. Sci. Eng., 138(4), p. 041003.
[6] Wang, M., Ken, T., Du, S., and Xi, L., 2015, "Tool Wear Monitoring of Wiper Inserts in Multi-Insert Face Milling Using Three-Dimensional Surface Form Indicators," ASME J. Manuf. Sci. Eng., 137(3), p. 031006.
[7] Wang, M., Shao, Y. P., Du, S. C., and Xi, L. F., 2015, "A Diffusion Filter for Discontinuous Surface Measured by High Definition Metrology," Int. J. Precis. Eng. Manuf., 16(10), pp. 2057–2062.
[8] Wang, M., Xi, L., and Du, S., 2014, "3D Surface Form Error Evaluation Using High Definition Metrology," Precis. Eng., 38(1), pp. 230–236.
[9] Suriano, S., Wang, H., Shao, C., Hu, S. J., and Sekhar, P., 2015, "Progressive Measurement and Monitoring for Multi-Resolution Data in Surface Manufacturing Considering Spatial and Cross Correlations," IIE Trans., 47(10), pp. 1033–1052.
[10] Nguyen, H. T., Wang, H., Tai, B. L., Ren, J., Hu, S. J., and Shih, A., 2016, "High-Definition Metrology Enabled Surface Variation Control by Cutting Load Balancing," ASME J. Manuf. Sci. Eng., 138(2), p. 021010.
[11] Cho, H., Luck, R., and Stevens, J. W., 2015, "An Improvement on the Standard Linear Uncertainty Quantification Using a Least-Squares Method," J. Uncertainty Anal. Appl., 3(1), pp. 1–13.
[12] Hongn, M., Larsen, S. F., Gea, M., and Altamirano, M., 2015, "Least Square Dased Method for the Estimation of the Optical End Loss of Linear Fresnel Concentrators," Sol. Energy, 111, pp. 264–276.
[13] Anselone, P., and Rall, L., 1968, "The Solution of Characteristic Value-Vector Problems by Newton's Method," Numer. Math., 11(1), pp. 38–45.
[14] Fischler, M. A., and Bolles, R. C., 1981, "Random Sample Consensus: A Paradigm for Model Fitting With Applications to Image Analysis and Automated Cartography," Commun. ACM, 24(6), pp. 381–395.
[15] Kim, T., and Im, Y. J., 2003, "Automatic Satellite Image Registration by Combination of Matching and Random Sample Consensus," IEEE Trans. on Geosci. Remote Sens., 41(5), pp. 1111–1117.
[16] Yaniv, Z., 2010, "Random Sample Consensus (RANSAC) Algorithm: A Generic Implementation," Insight Journal.
[17] Raguram, R., Chum, O., and Pollefeys, M., 2013, "USAC: A Universal Framework for Random Sample Consensus," IEEE Trans. Pattern Anal. Mach. Intell., 35(8), pp. 2022–2038.
[18] Leon, S. J., Björck, Å., and Gander, W., 2013, "Gram–Schmidt Orthogonalization: 100 Years and More," Numer. Linear Algebra Appl., 20(3), pp. 492–532.
[19] Pomerleau, F., Colas, F., Siegwart, R., and Magnenat, S., 2013, "Comparing ICP Variants on Real-World Data Sets," Auton. Rob., 34(3), pp. 133–148.
[20] Di Maio, F., Bandini, A., Zio, E., Alfonsi, A., and Rabiti, C., 2016, "An Approach Based on Support Vector Machines and a K-D Tree Search Algorithm for Identification of the Failure Domain and Safest Operating Conditions in Nuclear Systems," Prog. Nucl. Energy, 88, pp. 297–309.
[21] Schauer, J., and Nüchter, A., 2014, "Efficient Point Cloud Collision Detection and Analysis in a Tunnel Environment Using Kinematic Laser Scanning and KD Tree Search," Int. Arch. Photogramm. Remote Sens. Spat. Inf. Sci., 40(3), pp. 289–295.
[22] Besl, P. J., and McKay, H. D., 1992, "A Method for Registration of 3-D Shapes," IEEE Trans. Pattern Anal. Mach. Intell., 14(2), pp. 239–256.
[23] Du, S., and Xi, L., 2011, "Fault Diagnosis in Assembly Processes Based on Engineering-Driven Rules and PSOSAEN Algorithm," Comput. Ind. Eng., 60(1), pp. 77–88.
[24] Poli, R., Kennedy, J., and Blackwell, T., 2007, "Particle Swarm Optimization," Swarm Intell., 1(1), pp. 33–57.
[25] Coello, C. A. C., and Lechuga, M. S., 2002, "MOPSO: A Proposal for Multiple Objective Particle Swarm Optimization," IEEE Proceedings of the 2002 Congress on Evolutionary Computation, (CEC), Washington, DC, May 12–17, pp. 1051–1056.
[26] Reyes-Sierra, M., and Coello, C. C., 2006, "Multi-Objective Particle Swarm Optimizers: A Survey of the State-of-the-Art," Int. J. Comput. Intell. Res., 2(3), pp. 287–308.
[27] Zhang, Y., Gong, D., and Zhang, J., 2013, "Robot Path Planning in Uncertain Environment Using Multi-Objective Particle Swarm Optimization," Neurocomputing, 103, pp. 172–185.
[28] MVTec Software GmbH, 2010, "Halcon Solution Guide III-C 3D Vision," MVTec Software GmbH, München, Germany, http://download.mvtec.com/halcon-9.0-solution-guide-iii-c-3d-vision.pdf
[29] Dorsch, R., Häusler, G., and Herrmann, J., 1994, "Laser Triangulation: Fundamental Uncertainty in Distance Measurement," Appl. Opt., 33(7), pp. 1306–1314.